New Journal of Physics
The open access journal at the forefront of physics

Deutsche Physikalische Gesellschaft DPG IOP Institute of Physics

PAPER • OPEN ACCESS

# Optical properties of $In_2O_3$ from experiment and first-principles theory: influence of lattice screening

New Journal of Physics
The open access journal at the forefront of physics

Deutsche Physikalische Gesellschaft DPG
IOP Institute of Physics

Published in partnership with: Deutsche Physikalische Gesellschaft and the Institute of Physics

OPEN ACCESS

RECEIVED
15 January 2018

REVISED
24 March 2018

ACCEPTED FOR PUBLICATION
17 April 2018

PUBLISHED
4 May 2018



PAPER

# Optical properties of $In_2O_3$ from experiment and first-principles theory: influence of lattice screening

**André Schleife[1,2,3,8], Maciej D Neumann[4], Norbert Esser[4], Zbigniew Galazka[5], Alexander Gottwald[6], Jakob Nixdorf[7], Rüdiger Goldhahn[7] and Martin Feneberg[7]**

[1] Department of Materials Science and Engineering, University of Illinois at Urbana-Champaign, Urbana, IL 61801, United States of America
[2] Frederick Seitz Materials Research Laboratory, University of Illinois at Urbana-Champaign, Urbana, IL 61801, United States of America
[3] National Center for Supercomputing Applications, University of Illinois at Urbana-Champaign, Urbana, IL 61801, United States of America
[4] Leibniz-Institut für Analytische Wissenschaften—ISAS—e.V., Schwarzschildstraße 8, D-12489 Berlin, Germany
[5] Leibniz-Institut für Kristallzüchtung, Max-Born-Straße 2, D-12489 Berlin, Germany
[6] Physikalisch-Technische Bundesanstalt, Abbestraße 2-12, D-10587 Berlin, Germany
[7] Institut für Experimentelle Physik, Otto-von-Guericke-Universität Magdeburg, Universitätsplatz 2, D-39106 Magdeburg, Germany
[8] Author to whom any correspondence should be addressed.

**E-mail:** schleife@illinois.edu **and** martin.feneberg@ovgu.de

**Keywords:** excitonic effects, optical properties, ellipsometry, indium oxide, first-principles simulations

## Abstract

The framework of many-body perturbation theory led to deep insight into electronic structure and optical properties of diverse systems and, in particular, many semiconductors. It relies on an accurate approximation of the screened Coulomb electron–electron interaction *W*, that in current implementations is usually achieved by describing electronic interband transitions. However, our results for several oxide semiconductors indicate that for polar materials it is necessary to also account for lattice contributions to dielectric screening. To clarify this question in this work, we combine highly accurate experimentation and cutting-edge theoretical spectroscopy to elucidate the interplay of quasiparticle and excitonic effects for cubic bixbyite $In_2O_3$ across an unprecedentedly large photon energy range. We then show that the agreement between experiment and theory is excellent and, thus, validate that the physics of quasiparticle and excitonic effects is described accurately by these first-principles techniques, except for the immediate vicinity of the absorption onset. Finally, our combination of experimental and computational data clearly establishes the need for including a lattice contribution to dielectric screening in the screened electron–electron interaction, in order to improve the description of excitonic effects near the absorption edge.

## 1. Introduction

Modern first-principles theoretical spectroscopy has reached an unprecedented level of accuracy, due to methodological advances and the availability of high-performance supercomputers. In particular, the framework of many-body perturbation theory led to deep insight into optical properties of diverse systems, including molecules, one- and two-dimensional materials, as well as bulk semiconductors and insulators [1, 2]. By numerically solving approximations to Hedin's system of equations [3], this framework provides a systematic description of the electron–electron interaction. It enables accurate calculations of single-quasiparticle electronic excitations, such as band gaps, band structures, and densities of occupied and empty states. Many-body perturbation theory also allows to study two-particle excitations from first-principles, for instance bound electron–hole pairs, that are created when visible light is absorbed in a material. Such excitonic effects need to be taken into account in calculations of optical-absorption spectra and dielectric functions. Results for single- and two-particle excitations computed within many-body perturbation theory oftentimes agree very well with

**Table 1.** Experimental values of static ($\varepsilon_0$) and static *electronic* ($\varepsilon_\infty$) dielectric constants, exciton binding energies $E_B$ (in meV), and longitudinal-optical phonon frequencies $\nu_{LO}$ (in meV) of several semiconductors.

| Material | $\varepsilon_0$ | $\varepsilon_\infty$ | $E_B$ (meV) | $\nu_{LO}$ (meV) |
|---|---|---|---|---|
| Si | 11.7–12.1 [14] | 11.7–12.466 [15] | 15.01 [16] | 52.11 [17] |
| *wz*-GaN | 9.06 ($\perp c$), 10.04 ($\parallel c$) [18] | 5.16 ($\perp c$), 5.30 ($\parallel c$) [18] | 25.2 [19] | 91.9 ($\perp c$), 91.1 ($\parallel c$) [18] |
| *zb*-InN | — | 6.97 [20] | — | 72.9 [20] |
| *zb*-AlN | 8.07 [21] | 4.25 [21] | — | 111.2 [21] |
| *wz*-AlN | 7.65 ($\perp c$), 9.21 ($\parallel c$) [22] | 4.14 ($\perp c$), 4.34 ($\parallel c$) [22] | 55 [23] | 113.0 ($\perp c$), 110.3 ($\parallel c$) [22] |
| CaO | 12.01–12.2 [24] | 3.267–3.33 [24] | 104 [25] | 71.29 [26] |
| CdO | 21.9 [27] | 2.1, 5.3 [27] | — | — |
| MgO | 9.64–9.958 [28] | 2.944–3.179 [28] | 85 [25] | 89.00 [29] |
| ZnO | 7.8–11 [14, 30] | 3.7–4.0 [30] | 59.3–67.9 [31] | 72.41 [32] |
| $SnO_2$ | 7.031 [33]; 9, 14 [14] | 3.70 ($\perp c$), 3.90 ($\parallel c$) [34] | 33 [35] | 33.3, 41.5, 92.4 ($\perp c$), 83.1 ($\parallel c$) [36] |

experimental data, allowing for *quantitatively* accurate predictions and, eventually, computational materials design.

Accuracy and reliability of such predictions critically depend on underlying approximations that are necessary, in order to render calculations computationally feasible for real materials: In order to study single-particle excitations, Hedin's *GW* approximation has become widely adopted. It expresses the electronic self energy as product of the Green's function *G* and the screened electron–electron Coulomb interaction *W*. In practice, further approximations are needed and, while different schemes exist in the literature, the $G_0W_0$ approach, in which quasiparticle energies are computed as first-order perturbations, is most common [2]. Two-particle excitations, and specifically excitonic effects, are studied by solving a Bethe–Salpeter equation (BSE) for the optical polarization function. In this approach, *W* enters as the screened electron–hole interaction. It is, thus, important to obtain a reliable description of dielectric screening and of *W*, in order to accurately compute single- and two-particle excitations.

In numerical implementations of many-body perturbation theory, *W* is typically obtained using either the electronic structure from density-functional theory (DFT) and the random-phase approximation [4], or by parameterizing analytical model dielectric functions [1]. In both cases, the physical origin of the screening in *W* are electronic interband transitions. This approach has been very successful and can be considered state of the art [2]. We used it previously to provide highly accurate descriptions of electronic and optical properties of several semiconducting materials and, in particular, oxides [5–9].

More generally, optical spectra computed using many-body perturbation theory agree very well with experiment also for semiconductors such as silicon [1, 10], gallium nitride [11], and indium nitride [11]. We note that for these materials the values of static ($\varepsilon_0$) and static *electronic* ($\varepsilon_\infty$) dielectric constants are either both large or very close to each other (see table 1). When both dielectric constants are similar, electronic screening dominates even when exciton binding energies are smaller than longitudinal-optical (LO) phonon frequencies [12]. For some semiconductors that we studied previously, such as cubic aluminum nitride [13], calcium oxide [13], and cadmium oxide [5], excitonic effects and especially oscillator strengths of excitons near the band edge are very small both in simulation and experiment. This is likely due to the indirect fundamental band gap of these materials. AlN in the wurtzite structure is a direct semiconductor and was recognized as an 'intermediate case' before, because static and static *electronic* dielectric constants differ and exciton binding energies are smaller than LO phonon frequencies (see table 1 and [12]).

However, over the last few years we also studied several examples for semiconductors where comparison between experiment and theory points to deviations that are strongest in the vicinity of the absorption onset: for MgO [37], ZnO [5], and $SnO_2$ [6] we find that our computational results overestimate the strength of excitonic effects and, thus, their binding energy and oscillator strength near the band edge. For instance exciton binding energies computed for MgO overestimate experimental data by a factor of three.

These three oxides are so-called polar materials, as defined by a large splitting of longitudinal- and transverse-optical phonon frequencies. Via the Lyddane–Sachs–Teller relation [38, 39], this large splitting is evident from the large static dielectric constants compared to the much smaller static *electronic* dielectric constants (see table 1). The data in table 1 shows that for the polar materials the exciton binding energy is very close to LO phonon frequencies. This is also true for $In_2O_3$, for which the exciton binding energy is estimated to be 31 meV [40] and the LO phonon frequency is 27.8 meV [41]. For materials that show this behavior it is currently debated whether the electron–electron interaction is affected exclusively by electronic (interband)

screening, or whether a lattice contribution needs to be taken into account [39]. Here we will shed further light onto this question, by combining highly accurate experimentation with cutting-edge first-principles theoretical spectroscopy for one specific polar material: indium oxide, $In_2O_3$.

$In_2O_3$ is a transparent conducting oxide (TCO) and highly interesting both from a fundamental and applied point of view [42, 43]. It has, for instance, been successfully used for display applications, especially when combined with Ga and Zn to form indium–gallium–zinc oxide. However, $In_2O_3$ has proven challenging for experiment and theory: on the experimental side, difficulties arise from the need for high-quality, optically polished single crystals and a setup which allows for accurate determination of optical constants up to photon energies of 40 eV. Preparation of large enough single crystalline samples became possible only recently [44–46]. In addition, measuring the significant electronic contributions to the dielectric function of $In_2O_3$ up to photon energies of more than 30 eV, requires carefully prepared samples with particularly low surface roughness and high homogeneity.

Accurate computational studies, based on many-body perturbation theory, are demanding because the bixbyite polymorph of $In_2O_3$ found under ambient conditions requires a complicated 40-atom unit cell [47]. Computation of energy-dependent quasiparticle and excitonic effects for this many atoms up to high photon energies is computationally expensive. Consequently, detailed investigations of the fundamental optical properties of $In_2O_3$ appeared only recently: experiment focused on the spectral region around the absorption onset and into the visible range [40], as well as photon energies up to $\approx$10 eV [48]. First-principles simulations studied optical-absorption up to only slightly higher energies and analyzed the influence of excitonic effects near the absorption edge [49].

At the same time, $In_2O_3$ has a rich electronic structure that leads to significant amplitude and features in optical properties up to large photon energies. We use this as an excellent opportunity to validate first-principles theoretical spectroscopy across 0.5–40 eV and to develop a quantitative description of electronic and optical properties across this large energy range by combining high-quality experiment and cutting-edge theory. We disentangle quasiparticle and excitonic effects, investigate their energy dependence, and analyze their orbital contributions. Based on our data we show that the physics of quasiparticle and excitonic effects is described correctly when using a combination of hybrid exchange-correlation functionals and the Bethe–Salpeter approach.

Finally, we use our results to explore the underlying dielectric screening mechanism of the electron–hole interaction that dominates the optical-absorption onset. $In_2O_3$, like other TCOs discussed above (see table 1), is a polar material with a large static dielectric constant ($\varepsilon_0 = 8.9$, see [50]) and a small static *electronic* dielectric constant ($\varepsilon_\infty = 4.08$, see below). By comparing our experimental and computational results, we establish the need for a currently absent description of electronic *and* lattice contributions to dielectric screening.

The remainder of this work is structured as follows: the theoretical framework and computational approach is briefly described in section 2 and the experimental techniques are discussed in section 3. Experimental and theoretical spectra are presented and discussed in section 4. Finally, section 5 concludes our work.

## 2. Computational approach

We use DFT [51, 52] to compute Kohn–Sham states and eigenvalues as starting electronic structure for many-body perturbation theory. The generalized-gradient approximation by Perdew, Burke, and Ernzerhof [53] (PBE) is used to describe exchange and correlation. The electron–ion interaction is described using the projector-augmented wave method [54]. Kohn–Sham states are expanded into a plane-wave basis up to a cutoff energy of 400 eV and we use different randomly shifted **k**-point grids[9] for optical spectra, unless explicitly stated otherwise.

All calculations are carried out using the Vienna *ab initio* Simulation Package [55–57] and the BSE implementation discussed in [37, 58]. We adopt the atomic geometries relaxed with the HSE06 hybrid functional [59], as reported in [60].

### 2.1. Quasiparticle energies

It is well-known that DFT does not provide an accurate description of single-particle excitation energies, since it neglects quasiparticle effects. This manifests itself most famously in a severe underestimation of band gaps within DFT, compared to experiment. Furthermore, it is known that correcting the band gap and energies of higher conduction bands merely by applying a rigid scissor shift $\Delta$ is not sufficient: In particular, for various TCOs we previously showed that while this approximation works well in the vicinity of the absorption onset, it

[9] The spectrum between 0 and 9.18 eV is computed using a $5 \times 5 \times 5$ randomly shifted **k**-point grid and a BSE cutoff of 12.5 eV. The second part between 9.18 and 15.54 eV is computed using a $4 \times 4 \times 4$ randomly shifted mesh and a BSE cutoff of 17.0 eV. Finally, a BSE cutoff of 40.0 eV and $2 \times 2 \times 2$ randomly shifted points are used for higher photon energies.

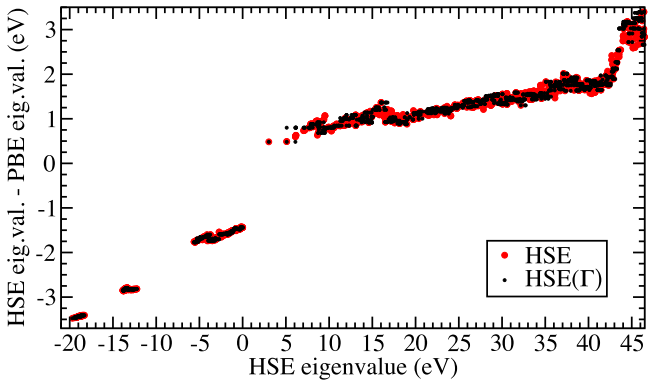


**Figure 1.** Quasiparticle shift for DFT-PBE eigenvalues, plotted as a function of the corresponding HSE eigenvalue. This data was computed using a 2 × 2 × 2 Gamma centered Monkhorst–Pack **k**-point grid.

increasingly underestimates the energies of bands the higher they appear in the band structure. Specifically in the case of ZnO we found significant deviations already at energies around 8.9 eV and higher [5], i.e. at significantly lower energies than what we study in this work. The slope behavior of the quasiparticle corrections visible in figure 1 illustrates this problem for $In_2O_3$.

In order to provide an accurate description of the single-particle electronic structure, Hedin's *GW* approximation [1–3] for the electronic self energy approximates quasiparticle effects very well for most TCOs. However, while yielding accurate results both for band gaps and band dispersion of these materials [5, 6, 47, 61, 62], this approach is computationally very expensive. In particular for complicated materials, such as $In_2O_3$ with a unit cell of 40 atoms, it becomes unaffordable even on modern supercomputers [47]. In the present work this situation is exacerbated since we aim at a description of optical transitions up to 40 eV, which requires a large number of bands and **k**-points, leading to significant computational cost even on DFT level.

In order to achieve an accurate, energy-dependent description of quasiparticle energies and, at the same time, circumvent the unaffordably high computational cost of *GW* calculations, we rely on the HSE06 hybrid functional [59] in this work. Using this functional to describe exchange and correlation has been shown previously to provide a reliable description of the band structure and density of states for $In_2O_3$ [60], at a computational cost that is lower than that of the *GW* method.

Unfortunately, in the context of this work, the hybrid HSE06 exchange-correlation functional is still too expensive to explicitly use it for converging optical spectra (see details below as well as (see footnote 8)). Instead we employ the following approach: first we compute approximate quasiparticle energies using HSE06 on a less dense 2 × 2 × 2 Gamma centered Monkhorst–Pack **k**-point grid [63]. Next, we compute the energy difference of each band at the Γ point of the Brillouin zone with respect to the DFT-PBE band energy. These results are called HSE(Γ) in the following and in order to verify this approach, we compare those to the fully **k**-dependent HSE results in figure 1. This illustrates that the HSE(Γ) approximation provides a reasonable approximation for single-particle energies for $In_2O_3$.

For converged calculations of optical spectra, we then use this data as a band-dependent scissor shift, and compare to the typically used band-independent scissor shift Δ. As we will discuss below, the HSE(Γ) approach allows us to more accurately take quasiparticle effects into account than the simple scissor operator. Yet the computational cost remains moderate for the dense **k**-point grids used in this work to compute converged optical-absorption spectra.

### 2.2. Optical properties: non-interacting electron–hole pairs

We focus on the complex, frequency-dependent dielectric function to represent the full linear optical response of cubic bulk bixbyite $In_2O_3$. To determine the importance of excitonic effects within this work, we compute this quantity across a photon energy range from 0.5 to 40 eV both using the single-quasiparticle approximation as well as the BSE approach. The former technique treats electrons and holes as non-interacting, while the latter takes their (screened) Coulomb interaction into account. Quasiparticle effects are approximated by the scissor operator Δ as well as the HSE(Γ) approach. Optical transition-matrix elements are computed from the Kohn–Sham electronic structure using the longitudinal approximation [55]. Using the Ehrenreich–Cohen formula [64], the imaginary part of the dielectric tensor then follows as [55]

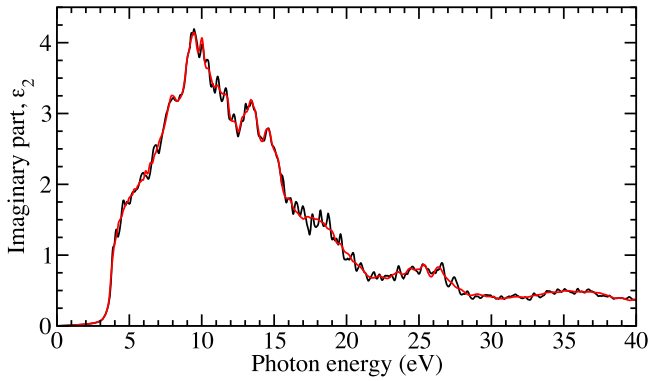


**Figure 2.** Independent electron–hole pair spectrum computed using a single **k**-point grid (red) and by joining spectra computed for different Brillouin zone sampling (black). Details see text and footnote 9.

$$\varepsilon_i^{\alpha\beta}(\omega) = \frac{4\pi^2 e^2}{\Omega} \lim_{q\to 0} \frac{1}{q^2} \sum_{c,v,\mathbf{k}} 2w_{\mathbf{k}}\, \delta(E_{c\mathbf{k}} - E_{v\mathbf{k}} - \omega) \times \langle u_{c\mathbf{k}+\mathbf{e}^\alpha q} | u_{v\mathbf{k}} \rangle \langle u_{v\mathbf{k}} | u_{c\mathbf{k}+\mathbf{e}^\beta q} \rangle^*. \quad (1)$$

In equation (1), $u_{n\mathbf{k}}$ represent cell-periodic parts of the Bloch wave functions and **q** is the Bloch wave-vector of incident light. The indices $c$ and $v$ describe conduction and valence band states, respectively. Provided the imaginary part is known up to high energies, the real part of $\varepsilon_i^{\alpha\beta}(\omega)$ can be obtained using a Kramers–Kronig transform [65, 66]. Due to the cubic symmetry of $In_2O_3$, the dielectric tensor has only one independent component, i.e. the dielectric function.

The sum over both valence and conduction bands as well as k-points in equation (1) illustrates why it is complicated to compute converged optical spectra up to high photon energies: we found that a $12 \times 12 \times 12$ Monkhorst–Pack **k**-point grid [63] yields a smooth dielectric function in the case of bixbyite $In_2O_3$ (red curve in figure 2). At the same time, computing optical spectra up to photon energies of 40 eV requires inclusion of a large number of electronic states above and below the fundamental gap. Fulfilling both of these requirements simultaneously causes significant computational cost even for independent electron–hole pairs; this becomes unfeasible on modern supercomputers, especially when excitonic effects are included.

Fortunately, the convergence criteria at low (a few eV above the band edge) and higher photon energies are complementary: at low energies, a very dense **k**-point sampling is required while only few electron and hole states around the fundamental band gap are needed. Contrary, for high photon energies inclusion of a large number of bands is required, but more coarse **k**-point grids are sufficient. This allows us to use different **k**-point meshes and numbers of bands for independent electron–hole pairs to compute different energy regions of the dielectric function. To verify this approach, we use the parameters listed in footnote 8 along with a scissor operator $\Delta = 1.8$ eV (see [49]) and compare to the converged result in figure 2. This clearly shows that the difference between these two approaches is very small, which indicates that the **k**-point grids described in footnote 8 produce converged results. While the joint spectrum is slightly less smooth, it comes at significantly reduced computational cost that will allow including excitonic effects by means of many-body perturbation theory (see section 2.3).

### 2.3. Optical properties: excitonic effects

We take excitonic and local-field effects into account by solving a BSE for the optical polarization function [1]. In practice, this amounts to solving an eigenvalue problem for the exciton Hamiltonian,

$$H(cv\mathbf{k},\, c'v'\mathbf{k}') = (\varepsilon_{c\mathbf{k}}^{\mathrm{QP}} - \varepsilon_{v\mathbf{k}}^{\mathrm{QP}})\delta_{cc'}\, \delta_{vv'}\, \delta_{\mathbf{k}\mathbf{k}'} - \Xi(cv\mathbf{k},\, c'v'\mathbf{k}'), \quad (2)$$

where $\Xi$ is the kernel of the BSE that contains both the statically screened Coulomb attraction as well as the unscreened exchange terms of the Coulomb electron–electron interaction of electron–hole pairs. Single-quasiparticle energies of conduction and valence bands, $\varepsilon_{c\mathbf{k}}^{\mathrm{QP}}$ and $\varepsilon_{v\mathbf{k}}^{\mathrm{QP}}$ respectively, appear on the diagonal of this Hamiltonian.

Despite using the **k**-point grids described in footnote 8 these calculations lead to extremely large ranks of the exciton Hamiltonians, up to 377, 565 in this work. This requires large memory (up to 1 terabyte) and can only be achieved on modern supercomputers such as Blue Waters. Still, a direct diagonalization of the Hamiltonian is numerically too expensive. Instead we use a time-propagation technique that scales quadratically with the rank of the Hamiltonian [67, 68].

### 2.4. Dielectric screening

Finally, the kernel $\Xi$ of the BSE, equation (2), requires computation of the screened electron–electron interaction $W$ [1]. In practice, the static (frequency independent, but wave-vector dependent) approximation is used for BSE calculations, where the screening is expressed as the inverse of the dielectric function $\varepsilon(q)$. This quantity can be computed directly from the Kohn–Sham electronic structure within the random-phase approximation [4]. To reduce computational cost, we express $\varepsilon(q)$ using the analytical model function by Bechstedt *et al* [69] This allows us to avoid the computationally expensive numerical inversion of $\varepsilon(q)$, by computing the inverse analytically. This is crucial to achieve converged BSE calculations for $In_2O_3$ up to large photon energies.

The analytical model [69] requires the dielectric constant of the material as a parameter and typically the static *electronic* dielectric constant computed within DFT is used, which is $\varepsilon_\infty = 4.80$ in the case of $In_2O_3$. This value is fairly close to the experimental result of 4.08 determined in this work (see section 4.1). The deviation can be attributed to the DFT band gap underestimation, which, via the Kramers–Kronig relation, leads to a too large static *electronic* dielectric constant.

However, we mentioned earlier that the *static* dielectric constant, that includes lattice contributions, is much larger ($\varepsilon_0 = 8.9$, see [50]) for $In_2O_3$. The Lyddane–Sachs–Teller relation [38] connects this difference of the dielectric constants to a large splitting of the longitudinal- and transverse-optical phonons:

$$\frac{\omega_{\mathrm{LO}}^2}{\omega_{\mathrm{TO}}^2} = \frac{\varepsilon_0}{\varepsilon_\infty}. \tag{3}$$

This illustrates the polar character of $In_2O_3$, which affects the electron–electron interaction $W$, as has been shown using quasiparticle energies in [39]. Since the screened electron–electron interaction also determines exciton binding and, thus, the strength of excitonic effects, the polar character should directly be reflected in the optical properties of the material.

In order to study this effect for $In_2O_3$, we take lattice screening into account using the approach outlined in [12]. This amounts to using the static dielectric constant to parameterize the model dielectric function, instead of the static *electronic* dielectric constant $\varepsilon_\infty$. While the static dielectric constant can be computed from first-principles, we use the experimental value of $\varepsilon_0 = 8.9$ in this work [50]. This overestimates lattice contributions to the screening, however, we use this approach here as a first approximation to clearly establish the need for a more accurate approach for these contributions in the description of the screened electron–electron interaction.

## 3. Experimental techniques

A cubic bixbyite 111 oriented $In_2O_3$ bulk sample (bulk crystal growth details can be found in [46]) with $n_{\mathrm{Hall}} = 3.7 \times 10^{17}\ \mathrm{cm}^{-3}$ and $\mu_{\mathrm{Hall}} = 114\ \mathrm{cm}^2\ \mathrm{V}^{-1}\ \mathrm{s}^{-1}$ was selected. The sample is of very high crystalline quality as mirrored by x-ray diffraction published earlier. The $\omega$-scan of the (222) reflex yields a full-width of half maximum around 28 arcsec [45]. As demonstrated in [40] for the sample studied here, the spectral dependence of the dielectric function around the absorption edge is well described by model functions of indirect and dipole-allowed excitonic contributions with characteristic energies of 2.75 eV and 3.8 eV, respectively. The preferred experimental technique allowing the dielectric function to be determined accurately is spectroscopic ellipsometry. In order to cover the spectral range of photon energies required for this study, a unique vacuum ultraviolet synchrotron-radiation-based spectroscopic ellipsometer was used, which is installed at the insertion device beamline of the metrology light source (MLS), a synchrotron-radiation facility of the Physikalisch-Technische Bundesanstalt in Berlin, Germany. A detailed description of technical possibilities, limitations, and specifications of the instrument is published elsewhere [70].

The sample was measured at different angles of incidence in different spectral regions to allow optimal signal-to-noise ratio. Between $\hbar\omega = 5$ and 10 eV, the angle of incidence $\phi$ was 67° and for 10 eV $< \hbar\omega <$ 40 eV $\phi$ was 52.9° and 52.7°.

In the lower photon energy range (0.5–6.5 eV) a conventional laboratory-based spectroscopic ellipsometer (Woollam VASE) with autoretarder was employed at two different $\phi$ (60° and 53°). Surface roughness was taken into account using the Bruggeman effective medium approximation with layer thickness of 2.7 nm. This correction also approximately accounts for possible existence of a thin electron accumulation layer. A dielectric function without assuming a line shape was fitted over the whole spectral range yielding the real and imaginary parts of the dielectric function as a function of photon energy $\bar{\varepsilon}(\hbar\omega) = \varepsilon_1(\hbar\omega) + i\varepsilon_2(\hbar\omega)$. The result was tested for Kramers–Kronig consistency by transforming imaginary and real parts separately and compare to numerically obtained results.

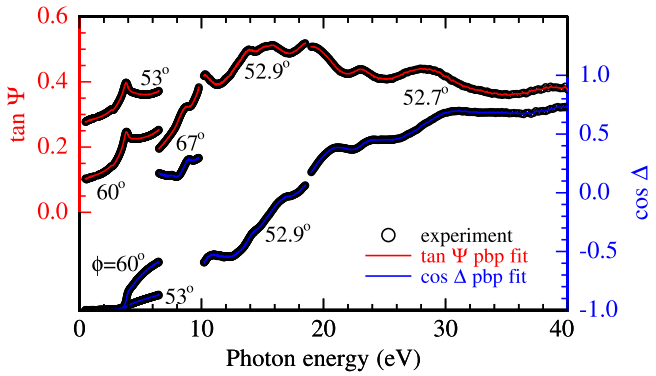


**Figure 3.** Comparison of experimental data (black circles) given as tan Ψ and cos Δ and corresponding point-by-point fitted model (continuous lines). The different angles of incidence $\phi$ for the different spectral regions are indicated within the plot.

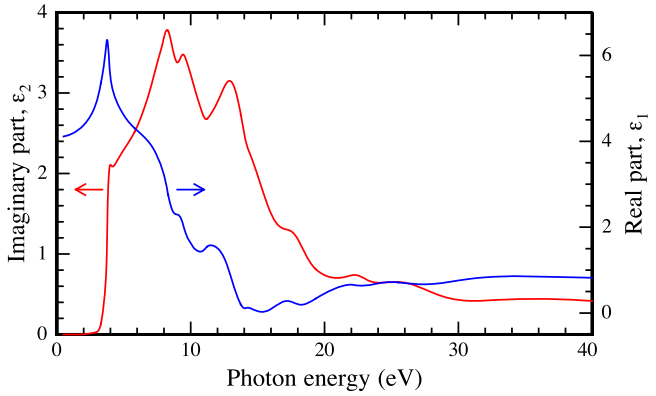


**Figure 4.** Experimental result for real (blue) and imaginary part (red) of the dielectric function.

## 4. Results and discussion

### 4.1. Experimental spectra

The experimentally obtained ellipsometric angles Ψ and Δ are used to define the ratio of Fresnel's coefficients $r_p$ and $r_s$ where the index marks the polarization direction ($p$ parallel, $s$ perpendicular) with respect to the plane of incidence:

$$\rho = \frac{r_p}{r_s} = \tan\Psi e^{i\Delta}. \tag{4}$$

The combined data for several angles of incidence $\phi$ compiled from both experimental instruments is shown in figure 3. The correction for surface roughness as discussed above yields the experimental complex dielectric function as shown in figure 4. As can be seen, a significant contribution to the imaginary part $\varepsilon_2$ of the dielectric function is located at very high photon energies $\hbar\omega > 15$–$20$ eV. This makes a use of the synchrotron ellipsometer mandatory. Please note that the low-energy region of the dielectric function ($\hbar\omega < 6.5$ eV) coincides with our earlier result from [40]. The *electronic* dielectric constant, determined as

$$\varepsilon_\infty = \lim_{\hbar\omega\to 0} \varepsilon_1$$

is found to be $4.08 \pm 0.02$ [40].

### 4.2. Computed spectra

Comparing highly accurate ellipsometry data for the complex dielectric function $\varepsilon(\omega)$ across such a large photon energy range to results from first-principles many-body perturbation theory is a rare opportunity for any material. Here we separately investigate the energy dependence of excitonic and quasiparticle effects to illustrate how both affect the dielectric function of $In_2O_3$. To this end, figure 5(a) shows the comparison of the experimental result and two computational spectra.

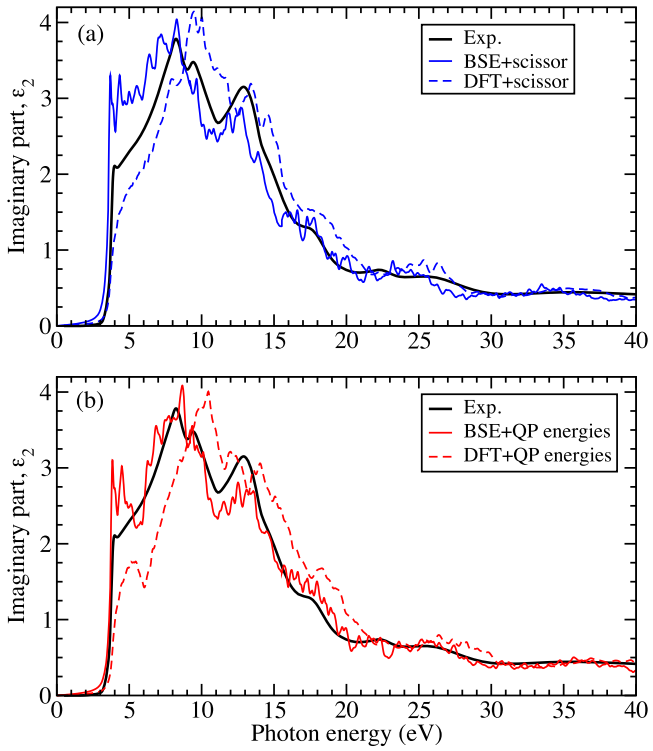


**Figure 5.** Imaginary part of the dielectric function computed with ('BSE', thin solid lines) and without ('DFT', dashed lines) excitonic effects, compared to the experimental result (thick solid black lines). In (a) merely a scissor operator ($\Delta = 1.8$ eV, see [49]) is used to approximate quasiparticle effects, and in (b) this is achieved using the HSE(Γ) approach.

This figure illustrates that excitonic effects cause the amplitude of $\varepsilon_2$ at the absorption edge to be almost twice as large, compared to the data where electron–hole interaction is neglected. We attribute the spectral feature at the onset to the lowest electron–hole excitation, which is an excitonic state with large oscillator strength. In addition, high-energy peaks appear red-shifted: One peak that is located around 9.8 eV in the DFT + Δ spectrum, occurs close to 8.3 eV when excitonic effects are included. Similar red shifts of about 1–1.5 eV are observed for structures around 13.5 eV (14.6 eV) that appear at 12.6 eV (13.9 eV) upon inclusion of excitonic effects. Even the small plateau-like feature at 17.05 eV is red-shifted to approximately 15.3 eV for the same reason. Both, the large oscillator strength of the lowest electron–hole excitation near the absorption onset and the red shift at larger photon energy due to electron–hole interaction are typical for many TCOs [5, 6, 49] and semiconductor materials.

In order to analyze the origin of peaks in the dielectric function, we compute the individual contributions from In 5*s*, 5*p*, 4*d*, as well as O 2*s* and O 2*p* states. To this end, figure 6 shows all transitions from those valence states into empty conduction-band states, as well as all transitions from all valence bands into those conduction states. This clearly indicates that the optical-absorption spectrum of $In_2O_3$ up to photon energies of about 22 eV is largely attributed to transitions that originate in O 2*p* valence bands. However, this figure also shows that significant spectral weight from In 4*d* valence states affects the dielectric function at energies above about 20 eV. Furthermore, these In 4*d* valence states are responsible for the peak-like structures around 25 eV.

Resolving the dielectric function with respect to conduction-band states supports and further details this picture. The absorption onset is clearly attributed to transitions into In 5*s* and O 2*p* states. At photon energies of about 10 eV the spectrum is dominated by optical transitions into In 5*p* bands. The spectral shape of these contributions resembles that of transitions into O 2*p* states, except for a shift to higher energies. As can be seen in figure 6, these In 5*p* states are responsible for the peak structures at around 25 eV. The shoulder near 20 eV can clearly be attributed to transitions into In 4*d*-derived bands. At even higher energies the dielectric function is dominated by transitions into In 4*d* states.

### 4.3. Quasiparticle and excitonic effects across large range of photon energies

Figure 5(a) also shows that the computational result from many-body perturbation theory agrees well with experiment, albeit not perfectly: we observe that in the energy range between 4 and 8 eV, the computational result noticeably overestimates experiment. Peaks around 8 eV agree very well, however, especially at high photon energies, it can be seen that the computational result underestimates the energy positions of peaks by

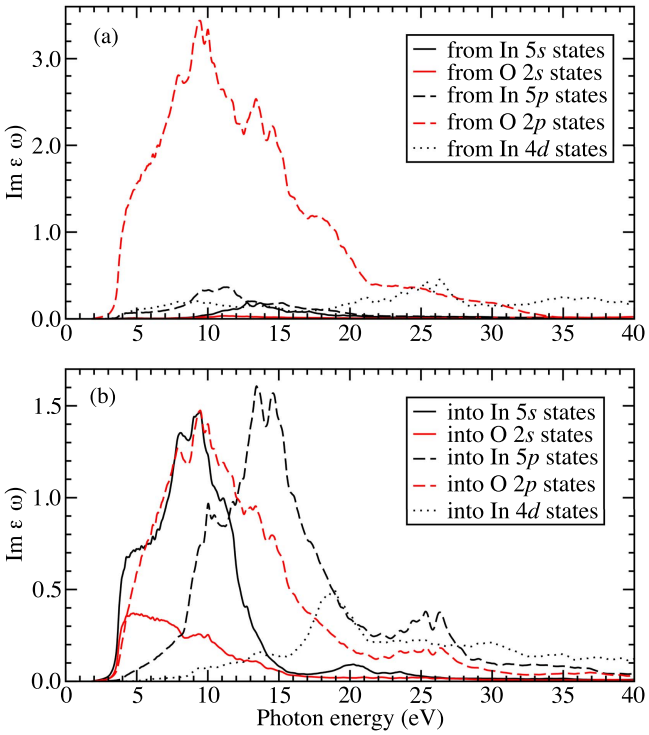


**Figure 6.** Ion- and angular-momentum-resolved dielectric function, computed within the DFT+scissor approximation. (a) Transitions from individual valence states into all conduction bands. (b) Transitions from all valence states into individual conduction bands.

approximately 0.7 eV (see e.g. the peak that occurs at 12.9 eV or the valley that appears at 11.2 eV in experiment). As we will show next, this can be attributed to the inadequate treatment of quasiparticle effects for high-lying conduction bands by the scissor operator. We also show that the HSE(Γ) approach significantly improves on this.

We first compare the scissor approach to HSE(Γ) for spectra that exclude excitonic effects (see dashed lines in figures 5(a) and (b)). The absorption onset appears at 2.9 eV when the scissor operator is used in figure 5(a) (matched to experimental data, see details in [49]), and at 3.02 eV in HSE(Γ) shown in figure 5(b). It can also be seen that the smooth increase of the dielectric function is replaced by a noticeable dip at 6.1 eV when the HSE(Γ) approach is used. This is attributed to transitions from oxygen 2*p* valence states into hybridized conduction-band states that consist of indium and oxygen *s* as well as oxygen *p* contributions.

As expected, for higher photon energies, we observe that peak positions computed within HSE(Γ) are at higher energies than accounted for by Δ. This indicates a clear energy dependence of quasiparticle corrections: Even if a scissor operator is used to correct for quasiparticle effects near the band gap, higher-energy bands would require a larger shift, since quasiparticle corrections for those are larger. At the same time, figure 5(b) clearly shows that excitonic effects are important and need to be included if the results are to be compared to experiment.

Finally, figure 5(b) also shows the comparison with experiment for the computational result that uses HSE (Γ) for quasiparticle effects and includes excitonic effects. It can be seen that this computational framework describes the experimental data for energies larger than ≈6 eV very accurately, regarding peak positions as well as amplitudes. Taking into account the energy dependence of quasiparticle effects noticeably improves agreement with experiment, especially at energies larger than ≈6 eV, as can be seen from the comparison with the dielectric function that includes excitonic effects but is based on a scissor operator (see figure 5(a)). This illustrates that an accurate description of quasiparticle effects, their energy dependence, and of excitonic effects is needed to successfully describe optical properties across a very large energy range.

Our results also show that for $In_2O_3$ the blue shift attributed to the energy dependence of quasiparticle effects and the red shift due to excitonic effects do not exactly compensate each other. Hence, there is no complete error cancellation that would justify approximating the high-energy part of the spectrum using a scissor-shifted DFT result.

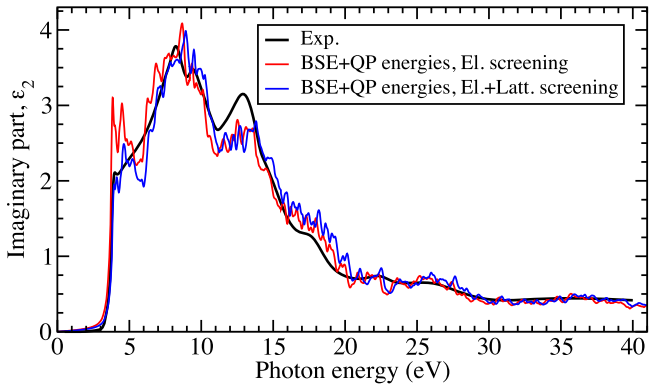


**Figure 7.** The imaginary part of the dielectric function, computed using two approaches to describe the screening of the electron–hole interaction (see text), is compared to our experimental data.

### 4.4. Influence of lattice screening

Having established the comparison of our experimental and computational results, we now use this data to analyze the influence of lattice screening: figure 5(b) shows that when excitonic and quasiparticle effects are included in the computational description, the remaining disagreement with experiment is largest in the vicinity of the optical-absorption onset: our result noticeably overestimates experiment up to photon energies of about 5.2 eV. More specifically, the BSE result that does not include any lattice screening overestimates experiment by a factor of approximately 1.3 in the vicinity of the absorption onset. Compared to this factor of 1.3 the spectrum that accounts for lattice screening shows merely a very minute difference from experiment. In the following we show that this can be explained by an influence of lattice screening on the electron–hole interaction.

It was reported before and discussed in section 2.4 that such an influence of lattice screening can, to zeroth order, be treated within the BSE framework by using the static dielectric constant instead of the static *electronic* dielectric constant in the model response function used to describe dielectric screening of the electron–hole interaction [12]. For the polar material $In_2O_3$, we follow this approach and use $\varepsilon_0 = 8.9$ instead of $\varepsilon_\infty = 4.80$ to parametrize the model dielectric function that describes the screened electron–hole interaction (see section 2.4) when computing the dielectric function shown in figure 7.

First, this result illustrates that the lattice contribution does not strongly affect the range of high photon energies. Above ≈10 eV the spectrum that results when the full lattice screening is taken into account strongly resembles the one for purely electronic screening. At the same time, figure 7 shows that lattice screening remarkably affects the low-energy range and strongly reduces the overestimation of peak amplitudes for photon energies up to about 5.2 eV that we criticized above. The agreement of the resulting spectrum with the experimental data is extremely good across the *entire* photon energy range from 0.5 to 40 eV.

More generally, we wish to point out that such an influence of lattice screening is not restricted to $In_2O_3$, but affects polar materials. If exciton binding energies are on the order of or smaller than the LO phonon frequency, and the static ($\varepsilon_0$) and static *electronic* ($\varepsilon_\infty$) dielectric constants differ, lattice contributions to dielectric screening are important [12]. These will reduce excitonic effects, i.e., lead to smaller exciton binding energy and smaller oscillator strength and we believe that this reduction can account for the overestimation of exciton binding energies within the BSE framework when just electronic screening is used (see e.g. [37]).

We note that in order to compute the blue curve in figure 7, we fully included the lattice contribution for all electron wave vectors $q$. This likely overestimates the lattice contribution, as discussed in [12], and could be the reason why the blue curve seems to slightly underestimate the experimental result, especially around 5.4–6.2 eV. Currently no full first-principles approach is available to go beyond the approximation used here. Our results, however, clearly emphasize the importance of such a technique and, while this goes beyond the scope of the present work, it is our goal to improve on this, e.g. by describing the correct $q$ dependence of the lattice screening contribution [39, 71] and to extend our work to more polar materials in the future.

## 5. Conclusions

In summary, we have used a combination of cutting-edge spectroscopic ellipsometry and first-principles many-body perturbation theory to investigate the dielectric function of bixbyite $In_2O_3$ over a very large photon energy range and to disentangle the influence of different atomic states. We showed that excellent *quantitative* agreement between experiment and computation is achieved when both quasiparticle and excitonic effects are

described as accurately as possible. We found a significant energy dependence of the quasiparticle corrections and used the HSE06 hybrid functional to accurately compute this effect at reasonable computational cost. We also found that excitonic effects influence the spectrum across the entire energy range and solved a BSE to take those into account. While this represents the most accurate comparison of cutting-edge experiment and predictive first-principles simulations of optical properties of $In_2O_3$, it also represents an important verification and validation step for both approaches.

Showing this excellent agreement is necessary to reliably interpret remaining deviations between experiment and simulation, which leads to the main insight of our work: we found that there is a significant disagreement for $In_2O_3$ that is most pronounced close to the absorption onset. We showed that this disagreement near the absorption onset can be tremendously reduced by including a lattice contribution to the screening of the electron–hole interaction, while leaving the good agreement at high photon energies unchanged. We thus demonstrate that it is necessary to accurately include both electronic and lattice contributions to dielectric screening in the description of the screened electron–electron interaction in polar semiconductors. Further experimental and theoretical research is needed to explore this effect for a larger set of polar semiconductors and to develop an accurate description of dielectric screening for this class of materials.

## Acknowledgments

We acknowledge fruitful discussions with F Bechstedt, C Bhandari, S Botti, W R L Lambrecht, and M A L Marques. Part of this work was supported by the National Science Foundation under Grant No. DMR-1555153. Financial support by the Senatsverwaltung für Wirtschaft, Technologie und Forschung des Landes Berlin, the Ministerium für Innovation, Wissenschaft und Forschung des Landes Nordrhein-Westfalen, and the Bundesministerium für Bildung und Forschung is acknowledged. Part of this work was performed within the framework of the Leibniz science campus GraFOx. This research is part of the Blue Waters sustained-petascale computing project, which is supported by the National Science Foundation (awards OCI-0725070 and ACI-1238993) and the state of Illinois. Blue Waters is a joint effort of the University of Illinois at Urbana-Champaign and its National Center for Supercomputing Applications.

## ORCID iDs

André Schleife https://orcid.org/0000-0003-0496-8214
Zbigniew Galazka https://orcid.org/0000-0003-0812-2873
Alexander Gottwald https://orcid.org/0000-0003-2810-7419
Rüdiger Goldhahn https://orcid.org/0000-0001-8296-2331
Martin Feneberg https://orcid.org/0000-0003-4253-0061

## References

[1] Onida G, Reining L and Rubio A 2002 *Rev. Mod. Phys.* **74** 601
[2] Louie S G 2006 *Predicting Materials and Properties: Theory of the Ground and Excited State* (Amsterdam: Elsevier) ch 2, pp 9–53
[3] Hedin L 1965 *Phys. Rev.* **139** A796
[4] Del Sole R and Girlanda R 1993 *Phys. Rev.* B **48** 11789
[5] Schleife A, Rödl C, Fuchs F, Furthmüller J and Bechstedt F 2009 *Phys. Rev.* B **80** 035112
[6] Schleife A, Varley J B, Fuchs F, Rödl C, Bechstedt F, Rinke P, Janotti A and Van de Walle C G 2011 *Phys. Rev.* B **83** 035116
[7] Schleife A, Rödl C, Fuchs F, Hannewald K and Bechstedt F 2011 *Phys. Rev. Lett.* **107** 236405
[8] Schleife A and Bechstedt F 2012 *J. Mater. Res.* **27** 2180
[9] Schleife A, Rinke P, Bechstedt F and Van de Walle C G 2013 *J. Phys. Chem.* C **117** 4189
[10] Albrecht S, Reining L, Del Sole R and Onida G 1998 *Phys. Rev. Lett.* **80** 4510
[11] de Carvalho L C, Schleife A, Furthmüller J and Bechstedt F 2013 *Phys. Rev.* B **87** 195211
[12] Bechstedt F, Seino K, Hahn P H and Schmidt W G 2005 *Phys. Rev.* B **72** 245114
[13] Riefer A, Fuchs F, Rödl C, Schleife A, Bechstedt F and Goldhahn R 2011 *Phys. Rev.* B **84** 075218
[14] Young K F and Frederikse H P R 1973 *J. Phys. Chem. Ref. Data* **2** 313
[15] Madelung O, Rössler U and Schulz M (ed) 2001 Silicon (Si) high-frequency dielectric constant *Group IV Elements, IV-IV and III-V Compounds. Part a - Lattice Properties* vol 41A1α (Berlin: Springer) (https://doi.org/10.1007/10551045_218)
[16] Green M A 2013 *AIP Adv.* **3** 112104
[17] 2002 Silicon (Si), phonon frequencies *Group IV Elements, IV-IV and III-V Compounds. Part b - Electronic, Transport, Optical and Other Properties* vol 41A1β (Berlin: Springer) (https://doi.org/10.1007/10832182_447)
[18] Feneberg M *et al* 2014 *Phys. Rev.* B **90** 075203
[19] Rodina A V, Dietrich M, Göldner A, Eckey L, Hoffmann A, Efros A L, Rosen M and Meyer B K 2001 *Phys. Rev.* B **64** 115204
[20] Schley P *et al* 2008 *Phys. Status Solidi* C **5** 2342
[21] Röppischer M, Goldhahn R, Rossbach G, Schley P, Cobet C, Esser N, Schupp T, Lischka K and As D J 2009 *J. Appl. Phys.* **106** 076104
[22] Feneberg M, Romero M F, Röppischer M, Cobet C, Esser N, Neuschl B, Thonke K, Bickermann M and Goldhahn R 2013 *Phys. Rev.* B **87** 235209

[23] Feneberg M, Leute R A R, Neuschl B, Thonke K and Bickermann M 2010 *Phys. Rev.* B **82** 075208
[24] Madelung O, Rössler U and Schulz M (ed) 1999 Calcium oxide (CaO) dielectric constants, optical properties *II-VI and I-VII Compounds; Semimagnetic Compounds* vol 41B (Berlin: Springer) (https://doi.org/10.1007/10681719_230)
[25] Whited R C and Walker W C 1969 *Phys. Rev. Lett.* **22** 1428
[26] Strauch D 2014 CaO: phonon frequencies *New Data and Updates for several IIa-VI Compounds (Structural Properties, Thermal and Thermodynamic Properties, and Lattice Properties)* vol 44G (Berlin: Springer) (https://doi.org/10.1007/978-3-642-41461-9_78)
[27] Madelung O, Rössler U and Schulz M (ed) 1999 Cadmium oxide (CdO) optical and photoelectric properties, dielectric constants, plasmon energy *II-VI and I-VII Compounds; Semimagnetic Compounds* vol 41B (Berlin: Springer) (https://doi.org/10.1007/10681719_515)
[28] Madelung O, Rössler U and Schulz M (ed) 1999 Magnesium oxide (MgO) dielectric constants, optical and photoelectric properties *II-VI and I-VII Compounds; Semimagnetic Compounds* vol 41B (Berlin: Springer) (https://doi.org/10.1007/10681719_213)
[29] 1999 Magnesium oxide (MgO) phonon dispersion and phonon frequencies: *II-VI and I-VII Compounds; Semimagnetic Compounds* vol 41B (Berlin: Springer) (https://doi.org/10.1007/10681719_207)
[30] Madelung O, Rössler U and Schulz M (ed) 1999 Zinc oxide (ZnO) dielectric constants *II-VI and I-VII Compounds; Semimagnetic Compounds* vol 41B (Berlin: Springer) (https://doi.org/10.1007/10681719_307)
[31] Meyer B K 2011 ZnO: exciton binding energies *New Data and Updates for IV-IV, III-V, II-VI and I-VII Compounds, their Mixed Crystals and Diluted Magnetic Semiconductors* ed U Rössler vol 44D (Berlin: Springer) (https://doi.org/10.1007/978-3-642-14148-5_332)
[32] Rössler U 2013 ZnO: phonon frequencies, mode-Grüneisen parameters *New Data and Updates for Several Semiconductors with Chalcopyrite Structure, for Several II-VI Compounds and Diluted Magnetic IV-VI Compounds* vol 44F (Berlin: Springer) (https://doi.org/10.1007/978-3-642-28531-8_80)
[33] Yıldırım M A, Yıldırım S T, Sakar E F and Ateş A 2014 *Spectrochim. Acta* A **133** 60
[34] Feneberg M, Lidig C, Lange K, White M E, Tsai M Y, Speck J S, Bierwagen O and Goldhahn R 2013 *Phys. Status Solidi* a **211** 82
[35] Fröhlich D, Kenklies R and Helbig R 1978 *Phys. Rev. Lett.* **41** 1750
[36] Xiang H, Lefkidis G and Hübner W 2012 *Phys. Rev.* B **86** 134402
[37] Fuchs F, Rödl C, Schleife A and Bechstedt F 2008 *Phys. Rev.* B **78** 085103
[38] Lyddane R H, Sachs R G and Teller E 1941 *Phys. Rev.* **59** 673
[39] Botti S and Marques M A L 2013 *Phys. Rev. Lett.* **110** 226404
[40] Feneberg M, Nixdorf J, Lidig C, Goldhahn R, Galazka Z, Bierwagen O and Speck J S 2016 *Phys. Rev.* B **93** 045203
[41] Sobotta H, Neumann H, Kühn G and Riede V 1990 *Cryst. Res. Technol.* **25** 61
[42] Nomura K, Ohta H, Takagi A, Kamiya T, Hirano M and Hosono H 2004 *Nature* **432** 488
[43] Ramirez A P 2007 *Science* **315** 1377
[44] Hagleitner D R *et al* 2012 *Phys. Rev.* B **85** 115441
[45] Galazka Z, Uecker R, Irmscher K, Schulz D, Klimm D, Albrecht M, Pietsch M, Ganschow S, Kwasniewski A and Fornari R 2013 *J. Cryst. Growth* **362** 349
[46] Galazka Z, Uecker R and Fornari R 2014 *J. Cryst. Growth* **388** 61
[47] Fuchs F and Bechstedt F 2008 *Phys. Rev.* B **77** 155107
[48] Schmidt-Grund R, Krauß H, Kranert C, Bonholzer M and Grundmann M 2014 *Appl. Phys. Lett.* **105** 111906
[49] Varley J B and Schleife A 2015 *Semicond. Sci. Technol.* **30** 024010
[50] Hamberg I and Granqvist C G 1986 *J. Appl. Phys.* **60** R123
[51] Hohenberg P and Kohn W 1964 *Phys. Rev.* **136** B864
[52] Kohn W and Sham L J 1965 *Phys. Rev.* **140** A1133
[53] Perdew J P, Burke K and Ernzerhof M 1996 *Phys. Rev. Lett.* **77** 3865
[54] Blöchl P E 1994 *Phys. Rev.* B **50** 17953
[55] Gajdoš M, Hummer K, Kresse G, Furthmüller J and Bechstedt F 2006 *Phys. Rev.* B **73** 045112
[56] Kresse G and Joubert D 1999 *Phys. Rev.* B **59** 1758
[57] Kresse G and Furthmüller J 1996 *Phys. Rev.* B **54** 11169
[58] Rödl C, Fuchs F, Furthmüller J and Bechstedt F 2008 *Phys. Rev.* B **77** 184408
[59] Heyd J, Scuseria G E and Ernzerhof M 2006 *J. Chem. Phys.* **124** 219906
[60] Varley J B, Peelaers H, Janotti A and Van de Walle C G 2011 *J. Phys.: Condens. Matter* **23** 334212
[61] Fuchs F, Furthmüller J, Bechstedt F, Shishkin M and Kresse G 2007 *Phys. Rev.* B **76** 115109
[62] Furthmüller J and Bechstedt F 2016 *Phys. Rev.* B **93** 115204
[63] Monkhorst H J and Pack J D 1976 *Phys. Rev.* B **13** 5188
[64] Ehrenreich H and Cohen M H 1959 *Phys. Rev.* **115** 786
[65] Kramers H A 1926 *Nature* **117** 775
[66] de R and Kronig L 1926 *J. Opt. Soc. Am.* **12** 547
[67] Hahn P H, Schmidt W G and Bechstedt F 2001 *Phys. Rev. Lett.* **88** 016402
[68] Schmidt W G, Glutsch S, Hahn P H and Bechstedt F 2003 *Phys. Rev.* B **67** 085307
[69] Bechstedt F, Sole R D, Cappellini G and Reining L 1992 *Solid State Commun.* **84** 765
[70] Neumann M D, Cobet C, Kaser H, Kolbe M, Gottwald A, Richter M and Esser N 2014 *Rev. Sci. Instrum.* **85** 055117
[71] Lambrecht W R L, Bhandari C and van Schilfgaarde M 2017 *Phys. Rev. Mater.* **1** 043802